



Failure characteristics and mechanism of a layered phyllite landslide triggered by foot excavation in the Qinba Mountains of China

Yanbo Cao^{1,2} · Longsheng Deng^{1,2,3} · Wen Fan^{1,2,3,4} · Dong Tang¹ · Jiale Chen¹ · Bin Zheng^{1,5}

Received: 20 March 2024 / Accepted: 14 August 2024 / Published online: 25 August 2024
© The Author(s) 2024

Abstract

China's Qinba Mountains Area presents a fragmented terrain, diverse geomorphology, and adverse geological structure. It is frequently impacted by severe geological hazards, especially in the weak rock strata of this area. The Yaobai landslide occurred on a slope with strong-moderately weathered phyllite and intensive structural planes, and foot excavation by human engineering activities triggered it. Large-scale physical model tests were carried out to elucidate the landslide's motion traits and damage mechanism by considering the influence of structural planes' inclination and orientation, filling conditions, slope foot excavation, etc. The results elucidated that the strength of the structural plane affected the ultimate angle of the slope foot and the location of the sliding plane; variation of structural plane orientation induced block rotations and increased the failure complexity; the mode of foot excavation affected the block slide sequence, locus, and distance. The landslide's deformation failure model can be summarized into three types: progressive sliding failure, monolithic sliding failure, and rotary sliding failure. The research results can provide a basis for preventing and controlling such landslides in the Qinba Mountains Area.

Keywords Large-scale physical model test · Foot excavation · Planar landslide in phyllite strata · Motion traits and failure mechanism of landslide

✉ Longsheng Deng
dlsh@chd.edu.cn

Yanbo Cao
caoyanbo@chd.edu.cn

Wen Fan
fanwen@chd.edu.cn

Dong Tang
tangdong@chd.edu.cn

Jiale Chen
chenjl@chd.edu.cn

Bin Zheng
zb5775@csepedi.com

¹ School of Geological Engineering and Geomatics of Chang'an University, Xi'an 710054, People's Republic of China

² Mine Geological Disasters Mechanism and Prevention Key Laboratory, Xi'an 710054, People's Republic of China

³ College of Civil Engineering and Mechanics of Lanzhou University, Lanzhou 730000, People's Republic of China

⁴ China Electronic Research Institute of Engineering Investigations and Design, Xi'an 710054, People's Republic of China

⁵ Central Southern China Electric Power Design Institute, Wuhan 430071, People's Republic of China

Introduction

Landslides are one of the most adverse geological hazards in the world, which can induce severe economic losses, threaten life safety, and impact environmental conditions catastrophically (Cruden 1991; Dai et al. 2002). Globally, such hazards have the potential for thousands of human casualties and billions of dollars of economic losses each year (Tsangaratos et al. 2017). The arising of landslides is exceedingly complex and significantly affected by various geological and environmental conditions.

The landslides are especially prone to occur in regions with intense geological tectonic activity. China's Qinba Mountains Area, which presents a fragmented terrain, diverse geomorphology, and adverse geological structure, is generally impacted by severe geological hazards. For instance, at 20:06 on July 18, 2010, the Zhaizigou landslide occurred in Qiyang Village, Dazhuyuan Town, Hanbin District of Ankang City. The landslide accumulation quickly turned into mudslides, leaving 29 people dead or missing, damaging 75 houses and causing economic losses of 2.73 million yuan (RMB) (Fan et al. 2019); On July 24, 2010, the Qiao Ergou landslide in Shanyang County, which

induced 6 people casualties, 18 people missing, 5 people injured, 53 houses destruction, caused the total economic losses amounting to 200 million yuan (RMB) (Wang et al. 2015); On August 12, 2015, a massive landslide occurred in Yanjiagou Village, Zhongcun Town, Shanyang County of Shaanxi Province, which buried 15 staff dormitories and 3 houses, causing 8 people dead and 57 people to go missing (Zhou et al. 2021). Similar hazards have occurred frequently in this area. According to the Shaanxi Provincial Geological Environment Monitoring Station statistics, 2699 geological hazards were recorded in the Qinba Mountains of Southern Shaanxi Province from 2001 to 2019, and most disaster events eventually induced severe hazards.

Landslide hazards have diverse inducing factors, complex triggering mechanisms, and variable disaster attributes, which make assessment, prevention, and control very difficult (Lan et al. 2022a). Researchers elucidate the failure traits, destabilizing mechanism, and damage model of landslides triggered by various external stimuli, such as earthquake (Cui et al. 2009; Keefer 1984; Qi et al. 2011; Tang et al. 2011; Yin et al. 2009), human activities (Li et al. 2020; Persichillo et al. 2018), intense rainfall (Fan et al. 2018; Fan et al., 2020 Yin et al. 2017), water level change, rapid stream erosion, etc. Existing research mainly focuses on disaster assessments for a specific area, with few in-depth analyses of individual landslide disasters. The primary focus is on rainfall-induced landslides. However, due to the shortage of land resources, slope foot excavation is extremely common in this area for building infrastructure. Studying the mechanisms and prevention/control of landslides under excavation conditions is of great significance.

Obtaining multiple fields of physical, stress, and deformation information in the slope is crucial for disaster and hazard assessment. Many theories, techniques, and methods are applied to research landslides in the field and laboratory. Field surveys and remote sensing interpretation can directly capture some of the essential characteristics exposed near the surfaces of the landslides and get part of the dynamic information through the comparative analysis of multi-timing images (Gao et al. 2020; Scaioni et al. 2014; Soldato et al. 2019; Xu et al. 2011, 2012; Xing et al. 2014). Despite obtaining excellent results, it is limited in exploring internal information about landslides. However, due to the steep terrain and dense, widespread vegetation in the Qinba Mountain Area, the application of existing survey and remote sensing interpretation technologies is significantly restricted. The deformations and multiple physical fields within the slope can be truly monitored through the buried sensors (Wei et al. 2019a, 2020); however, the monitoring point is limited and primarily applicable to small deformation and slow variation. Additionally, due to the influence of the characteristics of shallow sediment layers in the Qinba Mountain Area, the application of conventional multi-physical field

monitoring sensors may be affected, necessitating improvements in sensor accuracy, installation methods, and embedding techniques. Numerical simulation has advantages in considering complex conditions, but the reliability depends on the rationality and accuracy of boundary conditions, theoretical models, parameters, etc. (Wei et al. 2019b). Large-scale physical model tests can provide relatively reliable results, but design simplification can have adverse effects (Deng et al. 2018). Various methods have been widely used to obtain excellent research results, which paved the way for the effective prevention and control of geological disasters. Based on the strata and structure of the slopes, landslide disasters in the area are predominantly rockslides and shallow-layer landslides. In the simulations and tests, the effects of scale and internal structure are significant. However, existing research does not adequately consider these impacts.

Research on the landslide motion process is critical for hazard evaluation and risk prevention (Lan et al. 2022b). Tracking the variation of displacement, velocity, and acceleration of landslides is significant for evaluating energy state and transformation. On this basis, the impact force or energy can be estimated to retain the structure design, and the arrival distance and influence range can be determined for risk assessment. For example, rock avalanches' high mobility and long-runout potential, commonly quantified by the "apparent friction coefficient" or "angle of reach", still attract much attention to the complex mechanism and motion processes (Corominas 1996). Large and long-runout landslides are of societal concern because of their destructive power (Deng et al. 2020; Wang et al. 2018; Zhang et al. 2022). The research methods are mainly inversion analysis or simulation. Physical model experimentation to investigate kinematics involves rock landslides and studies of motion parameters and mechanisms to elucidate these phenomena (Alvarado et al. 2019; Iverson 2005; McDougall and Hungr 2004; Wang and Sassa, 2010). However, the high-precision quantitative monitoring of the moving process is still relatively limited, especially when the monitoring objects are large numbers and have significant speed and dramatic change in motion characteristics. There is an urgent need to develop experimental technologies and systems that can monitor the rapid motion of large landslide masses.

Soft rocks, such as schist, phyllite, mudstone, etc., are widely distributed in the Qinba Mountains. Landslides are especially prone to occur in areas with such soft strata because of the easy weathering and low-strength properties (Fan et al. 2019; Qiu et al. 2019). In addition, the rock structure surfaces are highly developed in the soft rock stratum, forming layer structural slopes, which are easily damaged by slope crest loading, foot excavation, and rainfall. In the Qinba Mountain Area, layer structure slope damage caused by foot excavation is widespread. The Yaobai landslide in Bailiu Town of Shaanxi Xunyang County occurred

in a layered phyllite slope with typical lithology, structure, deformation, and destruction characteristics.

This paper selects the Yaobai landslide as a specific research object. Through the field investigation, the geological engineering conditions of the landslide were explored, obtaining parameters for the research prototype. A large-scale physical model test was carried out to explore the transient block motion and elucidate the failure mechanism of the slope. The slope model was composed of many rock blocks with regular shapes. Monitoring and tracking many

blocks with high accuracy was complex, requiring precision monitoring systems. Consequently, a non-contact monitoring system is developed. The physical model experiment aimed to systematically explore the slope’s motion characteristics, deformation models, and failure mechanisms, considering the influence of joint planes’ inclination and orientation, filling conditions, slope foot excavation, etc. The research results can provide a basis for preventing and controlling such landslides. The research approach is shown in Fig. 1.

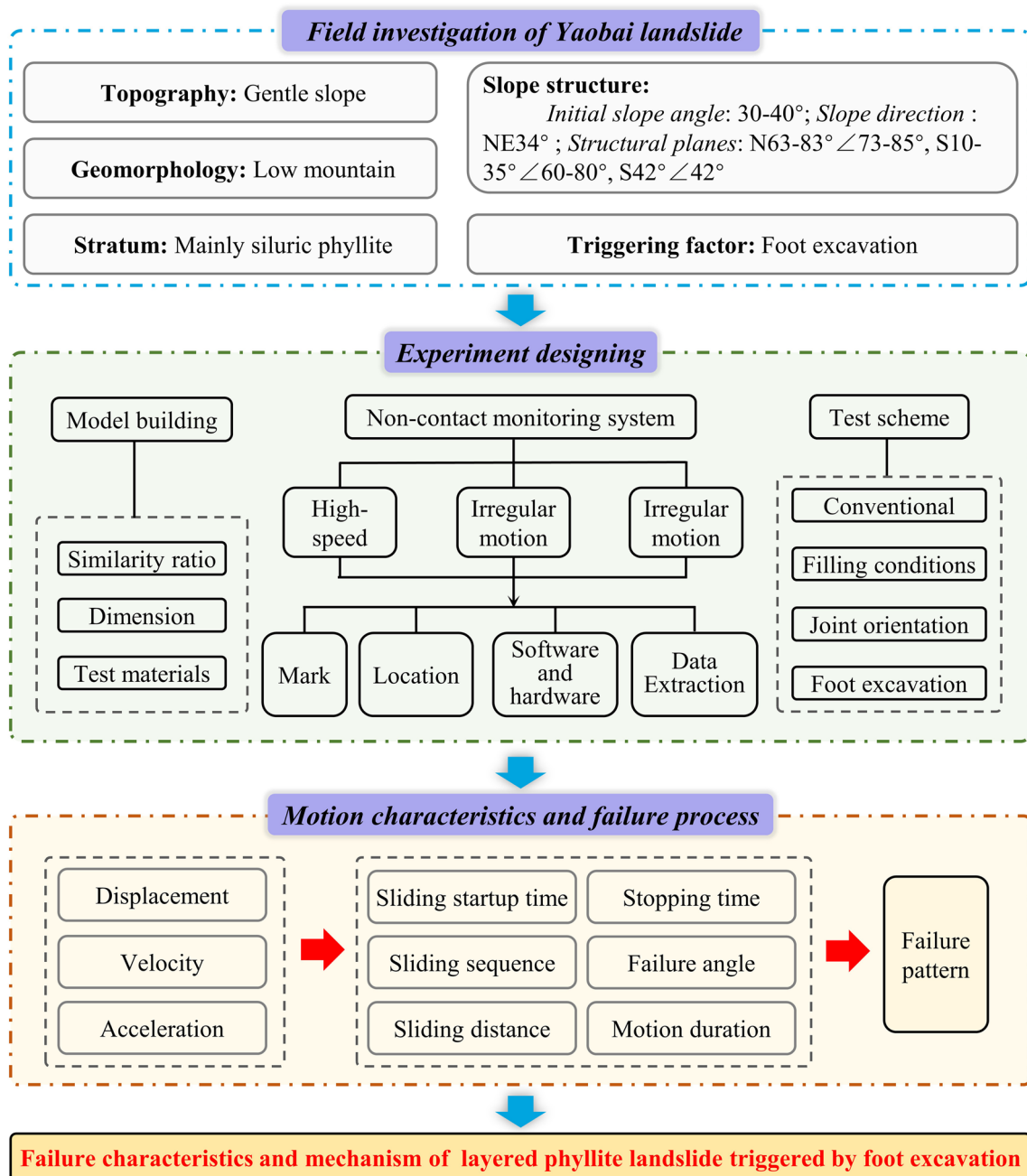


Fig. 1 Flow diagram of the research approach

Engineering geologic condition of the Yaobai landslide

Yaobai landslide (109°17'52.53"E, 32°49'53.41"N) is located in Bailiu Town of Shaanxi Xunyang County, where the geomorphology belongs to the Qinba low mountain regions. The stratum of the landslide is mainly Siluric phyllite in a layered formation structure, partially covered by a Quaternary deposit with a thickness of less than 30–50 cm. Three groups of structural planes developed in the rock mass, with the rock attitudes of N63–83°∠73–85°, S10–35°∠60–80°, and S42°∠42°, respectively. Most structural planes are closed, continuous, and dry, with a 0.2–0.6 m spacing and debris or mud filling. A Yaobai Cement Brick Factory excavated the slope toe to make bricks. The excavation region height is about 20 m, forming a free surface with a dip angle of about 50–60°. The initial slope angle is about 30–40° according to the inversion of the residual terrain on both sides of the slope. Until September 2020, the hill slid suddenly without any precursor information, and many blocks accumulated at the slope foot and caused severe disasters. The location and stratigraphic distribution are presented in Fig. 2.

The landslide altitude is 250 m for the toe and 314 m for the crown, respectively, and the height is about 64 m. The landslide orientation, inclination, and rear wall angle are 34°, 30–40°, and 70–80°, respectively. The landslide range is approximately a triangle with a length of 110 m and a

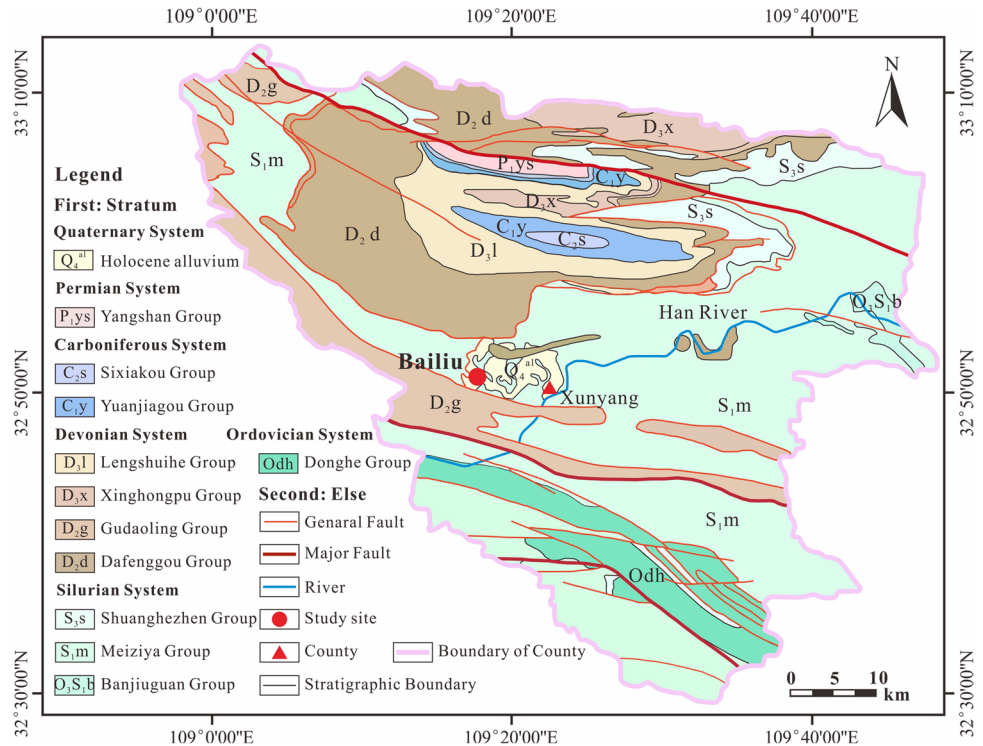
width of about 60 m. A residual excavation platform with a width of 3.0 m and a height of 20.0 m remained on the right front of the slope. The sliding surface area and landslide mass thicknesses are about 3300 m² and 5–7 m, respectively, with which the volume is about 16,500–23,100 m³. The geotechnical material of the landslide body is mainly rubble and rock blocks, with a proportion of more than 90%. The rock is composed of Silurian Sericite Phyllite. The block diameters varied along with the elevation, about 1.0–4.0 m in the upper part and 0.1–0.4 m in the lower part of the slope. The rock is moderately weathered, with a uniaxial compressive strength of 25.3 MPa. The Yaobai landslide belongs to a small landslide in scale.

Figure 3 presents essential characteristics of the Yaobai landslide. Table 1 shows the physical and mechanical parameters of the rock blocks and structural planes, which were obtained by adopting the triaxial compression test and direct shear test, respectively. The direct shear test was carried out by a large-scale rheological testing machine with a sample size of 35 × 35 × cm³.

Design of a non-contact monitoring system

Monitoring various landslide parameters is crucial for slope evaluation in the large-scale physical model test. Due to the particularity of this model test, it is necessary to monitor and track many blocks and capture their movement trajectory and fast movement process. However, the existing physical

Fig. 2 The location and geological environment conditions of the Yaobai landslide



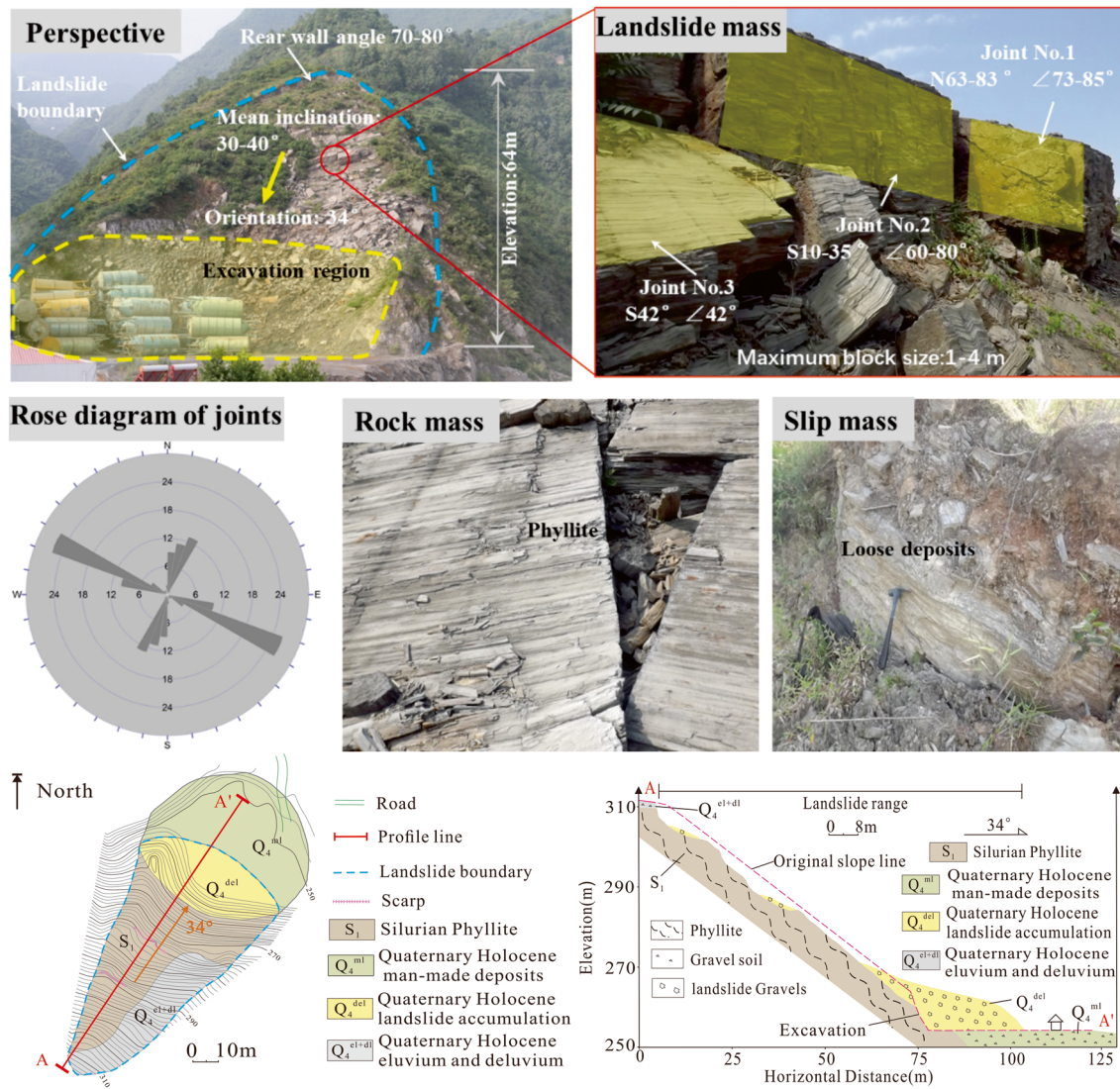


Fig. 3 Basic features of the Yaobai landslide

Table 1 Physical and mechanical parameters of materials for the test

Parameters	Unit of mass (g/cm ³)	Adhesion C (kPa)	Inner friction angle ϕ (°)	Young modulus E (GPa)	Poisson's ratio ν
Rock/ Model block	2.7	95.8	32.87	0.138	0.28
Structure plane	/	5.65	25.9	/	/

model test monitoring technology and system make it challenging to meet the needs of this test. Therefore, it is necessary to focus on the specific situation of the test technique.

A large-scale physical model test was carried out to explore the slope's motion features, influence factors, and failure mechanism. The physical model experiment aims to explore slope instability and block motion under specific

conditions, and blocks' displacements, velocities, and accelerations were highly significant. The slope model was composed of many regular blocks. Monitoring and tracking many blocks with high accuracy was a complex task requiring advanced monitoring systems. Consequently, developing a non-contact monitoring system is significant for the experiment.

Ring marks on the rock blocks

The traditional monitoring methods consider comparing texture image and elevation variation, which are poorly applicable to high-speed moving objects. The ring marks were widely used in close-range photogrammetry for the advantages of simple principle, convenient production, and excellent performance, which was finally selected as the identification logo for this study. The ring marks consist of three loops, and the ratio of the central circle radius and middle and outer bandwidths were designed to be 1:1:1, as shown in Fig. 4.

According to the Burnside Principle, the number of positive n edges painted with m colors can be calculated using the formula.

$$N = \frac{1}{n} \sum_{d|n} \phi(d)m^{n/d} \tag{1}$$

Where N is the number of ring marks; n is the number of circular encoding cells; $\phi(d)$ represents the co-prime number to parameter d ; m represents the number of painting colors. The value of N can be calculated as 2912 when $n = 15$, which is plenty to meet the encoding requirements for this experiment.

$$N = \frac{1}{15}(1 \times 2^{15} + 2 \times 2^5 + 4 \times 2^3 + 8 \times 2^1) = 2912 \tag{2}$$

The encoding and decoding formulas are specially designed to achieve the rotation-independent characteristics.

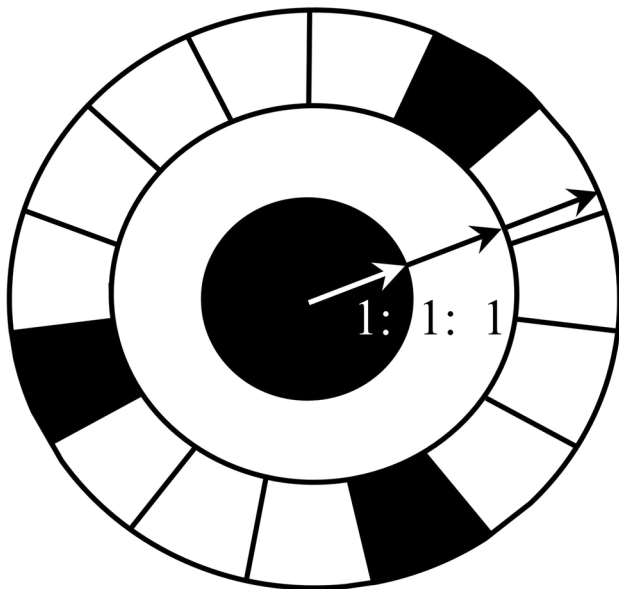


Fig. 4 Schematic diagram of the ring mark

$$P_{mark} = \min \left\{ p \in [0, 15] \sum_{i \in [0, 15]} 2^{(i+p) \% 15 v(i)} \right\} \tag{3}$$

Where i represents the position of the cell, ranging in $[0, 15]$; $v(i)$ represents the value of the cell at the i position, ranging in $\{0, 1\}$, and 0 for black and 1 for white; p represents the rotated angle.

The decoded information, marked on the surface of the rock blocks, is unique regardless of the rotation angle variation.

Auxiliary marks combination and identification of rock blocks

Determination of rock mass center based on auxiliary marks

Since block translation generally accompanies flip during landslide occurrence, the displacement-time curves drawn by adopting the block surface data were generally unstable. The auxiliary signs were designed to track the loci of rock centers, considering the prior local coordinate system relationship among the marks.

Figure 5 shows the design of auxiliary marks on block surfaces under the stereophotogrammetry system. Two coordinate systems were established, where O_1 in the left camera represents the global coordinates, and O_2 is the center of the rock block representing the local coordinate system. Red, blue, and green combinatorial colors marked the model block's front, side, and bottom surfaces. The ring code was stuck on specific surface centers. Color markers' local and spatial coordinates can be calculated accurately through image data.

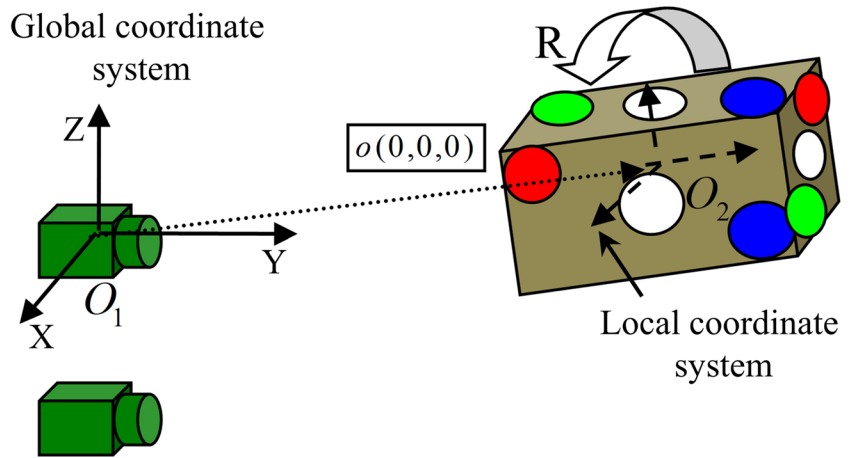
Set the block cuboid's length, width, and height as a , b , and c , respectively, and the circle radius of the auxiliary sign as r . Taking the front side marker combination matrix P_{before} as an example, the coordinates of each marker in the local coordinate system were described as the following formula (4).

$$P_{before} = \begin{bmatrix} P'_1 \\ P'_{mark} \\ P'_2 \end{bmatrix}^T = \begin{bmatrix} -\frac{a}{2} + r & 0 & \frac{a}{2} - r \\ \frac{b}{2} & \frac{b}{2} & \frac{b}{2} \\ \frac{c}{2} - r & 0 & -\frac{c}{2} + r \end{bmatrix} \tag{4}$$

Where P'_1 , P'_2 , and P'_{mark} are the coordinates vectors of the upper left, lower right auxiliary mark, and ring mark, respectively. Similarly, the local coordinate system coordinates for the ring marks, and additional marks on other sides of the block can be obtained.

Set the coordinate matrix P' of k marks that can be detected in the practical field of view as formula (5). The coordinates of detected color marks in the global system were represented as formula (6), combining the stereophotogrammetry system.

Fig. 5 Designing auxiliary marks of rock block (R denotes rotation)



$$P' = \begin{bmatrix} \overrightarrow{P'_{m_1}} & \dots & \overrightarrow{P'_{m_k}} \end{bmatrix} = \begin{bmatrix} x'_{m_1} & \dots & x'_{m_k} \\ y'_{m_1} & \dots & y'_{m_k} \\ z'_{m_1} & \dots & z'_{m_k} \end{bmatrix}_{3 \times k} \quad (5)$$

$$P = \begin{bmatrix} \overrightarrow{P_{m_1}} & \dots & \overrightarrow{P_{m_k}} \end{bmatrix} = \begin{bmatrix} x_{m_1} & \dots & x_{m_k} \\ y_{m_1} & \dots & y_{m_k} \\ z_{m_1} & \dots & z_{m_k} \end{bmatrix}_{3 \times k} \quad (6)$$

From the transformation relationship of the coordinate system,

$$P = R_x(\psi)R_y(\phi)R_z(\theta)(P' - L) = R(P' - L) \quad (7)$$

Where the function $R_x(\psi)$, $R_y(\phi)$, $R_z(\theta)$ are the rotation matrices of the rotation angles around the x, y, and z axes, respectively. L is the block mass center translation matrix.

$$L = \begin{bmatrix} l_x & \dots & l_x \\ l_y & \dots & l_y \\ l_z & \dots & l_z \end{bmatrix}_{3 \times k} \quad (8)$$

There are six unknown parameters, which are the rotation angle ψ , ϕ , θ , and translation parameters l_x , l_y , and l_z . Since one detectable marker circle center coordinates can provide three equations, only two detectable marker circle center coordinates are needed to obtain these six parameters. If there are more than two circle centers, the least-squares fitting can be performed to make the parameter calculation result more accurate.

Identification of marks based on Hough Circle Detection

The center of the circle for the auxiliary and ring marks on a specific side of the rock block are shown in Fig. 6. Image threshold segmentation and boundary extraction

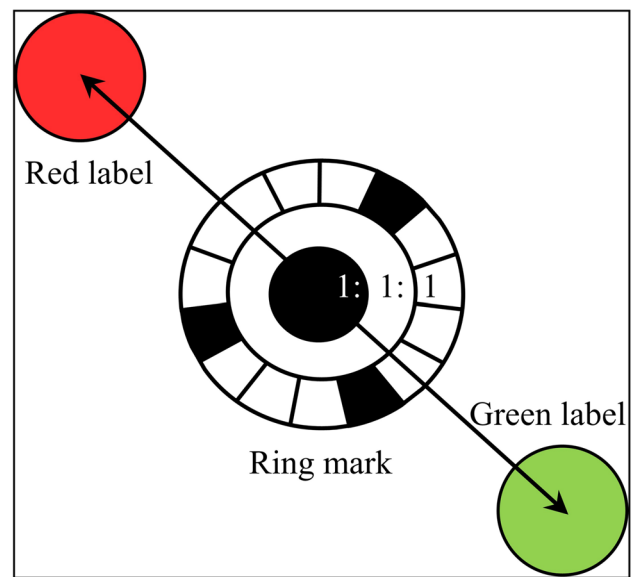


Fig. 6 Distribution of auxiliary marks and ring marks

methods were adopted to locate and identify the approximate position of the center of the circle. The Fast Hough Circle Detection method was adopted to identify the marks information.

The parametric equation of Hough Circle Detection is presented as follows.

$$\begin{cases} x = x_0 + r \cos \theta \\ y = y_0 + r \sin \theta \end{cases} \quad (9)$$

Where (x_0, y_0) is the center coordinates of the ring mark, which is a known coordinate value and can be determined according to the auxiliary marks. (x, y) is the target cell's coordinate after the ring mark's binarization. $0^\circ \leq \theta \leq 360^\circ$, $r = \frac{(y-x)-(y_0-x_0)}{\sin \theta - \cos \theta}$.

Traversing the set of (x, y) and θ , the candidate cumulative radius set $\{v_{r_i}\}_{i=1}^n$ was obtained. Since the ratio of the central circle radius and middle and outer bandwidths of the ring mark were designed to be 1:1:1, the actual radius of the ring mark can be calculated as.

$$r_{real} = \max(v_{r_i} + v_{2r_i} + v_{3r_i}) \tag{10}$$

The location and encoding of the ring marks were obtained through the center coordinates and the actual radius. The identification process based on the Hough Circle Detection method is shown in Fig. 7.

Extractions of block identification information and motion state

The identifications, spatial coordinates, and rotation angles of rock block centroids can be extracted based on image analysis of a specific frame image. The displacement, velocity, and acceleration of blocks in translation and rotation can be obtained by combining multi-frame image analysis.

Set the matrixes of spatial displacement, rotation angle, and the discrete-time vector to be $S, M,$ and \vec{T} , respectively, as shown in Eq. (11).

$$S = \begin{bmatrix} S_{11} & \dots & S_{n1} \\ \dots & \dots & \dots \\ S_{1m} & \dots & S_{nm} \end{bmatrix} = \begin{bmatrix} (x_{11}, y_{11}, z_{11}) & \dots & (x_{n1}, y_{n1}, z_{n1}) \\ \dots & \dots & \dots \\ (x_{1m}, y_{1m}, z_{1m}) & \dots & (x_{nm}, y_{nm}, z_{nm}) \end{bmatrix}$$

$$M = \begin{bmatrix} M_{11} & \dots & M_{n1} \\ \dots & \dots & \dots \\ M_{1m} & \dots & M_{nm} \end{bmatrix} = \begin{bmatrix} (\psi_{11}, \varphi_{11}, \theta_{11}) & \dots & (\psi_{n1}, \varphi_{n1}, \theta_{n1}) \\ \dots & \dots & \dots \\ (\psi_{1m}, \varphi_{1m}, \theta_{1m}) & \dots & (\psi_{nm}, \varphi_{nm}, \theta_{nm}) \end{bmatrix}$$

$$\vec{T} = [t_1 \dots t_m]^T \tag{11}$$

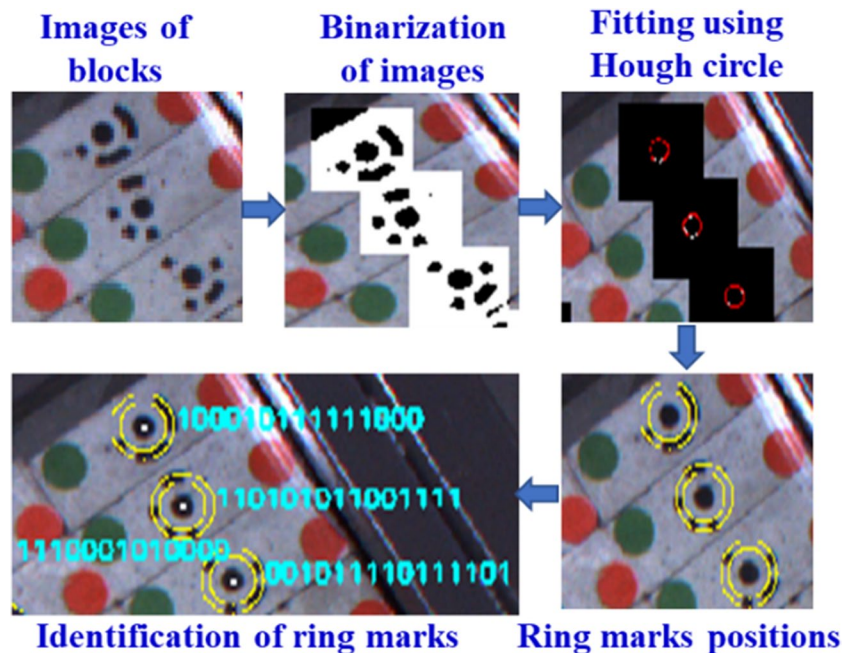
Where n and m are the number of landslide rock blocks and frames of discrete images, respectively. $x, y, z, \psi, \varphi, \theta$ represent the displacements and rotation angles. t is the time vector in the time domain.

The curves of blocks displacements, rotation angles, velocities, and accelerations are continuously converted from the discrete monitoring data, adopting the method of cubic polynomial interpolation. The displacement and rotation angle of the i^{th} rock block is presented in the expression (12), whereserial = α are the fitting parameters, and $t_1 \leq t \leq t_m$.

$$\begin{cases} x = x(t) = a_{x0} + a_{x1}t + a_{x2}t^2 + a_{x3}t^3 \\ y = y(t) = a_{y0} + a_{y1}t + a_{y2}t^2 + a_{y3}t^3 \\ z = z(t) = a_{z0} + a_{z1}t + a_{z2}t^2 + a_{z3}t^3 \\ \psi = \psi(t) = a_{\psi0} + a_{\psi1}t + a_{\psi2}t^2 + a_{\psi3}t^3 \\ \varphi = \varphi(t) = a_{\varphi0} + a_{\varphi1}t + a_{\varphi2}t^2 + a_{\varphi3}t^3 \\ \theta = \theta(t) = a_{\theta0} + a_{\theta1}t + a_{\theta2}t^2 + a_{\theta3}t^3 \end{cases} \tag{12}$$

Dynamically selected $S_{i(t_p-1)}, S_{i t_p}, S_{i t_q}, S_{i(t_q+1)},$ and $L_{i(t_p-1)}, L_{i t_p}, L_{i t_q}, L_{i(t_q+1)}$ as the interpolation points of displacement and

Fig. 7 Identification process based on the Hough Circle Detection method



rotation angle respectively, the continuous motion curves were calculated. The translational and the rotational velocity vector \vec{v}_t and \vec{m}_t are presented as follows.

$$\begin{aligned} \vec{v}_t &= \frac{\partial S}{\partial t} = \left(\frac{\partial x(t)}{\partial t}, \frac{\partial y(t)}{\partial t}, \frac{\partial z(t)}{\partial t} \right) \\ \vec{m}_t &= \frac{\partial M}{\partial t} = \left(\frac{\partial \psi(t)}{\partial t}, \frac{\partial \varphi(t)}{\partial t}, \frac{\partial \theta(t)}{\partial t} \right) \end{aligned} \quad (13)$$

Software and hardware

The image acquisition equipment consists of 3 industrial cameras, 64 G memory cards, wide-angle with a short focal lens. The software system consists of three modules: camera calibration, image acquisition, and displacement tracking. The number and code of marks can be generated randomly. An example of 3-D trajectory monitoring of the rock center of mass is shown in Fig. 8.

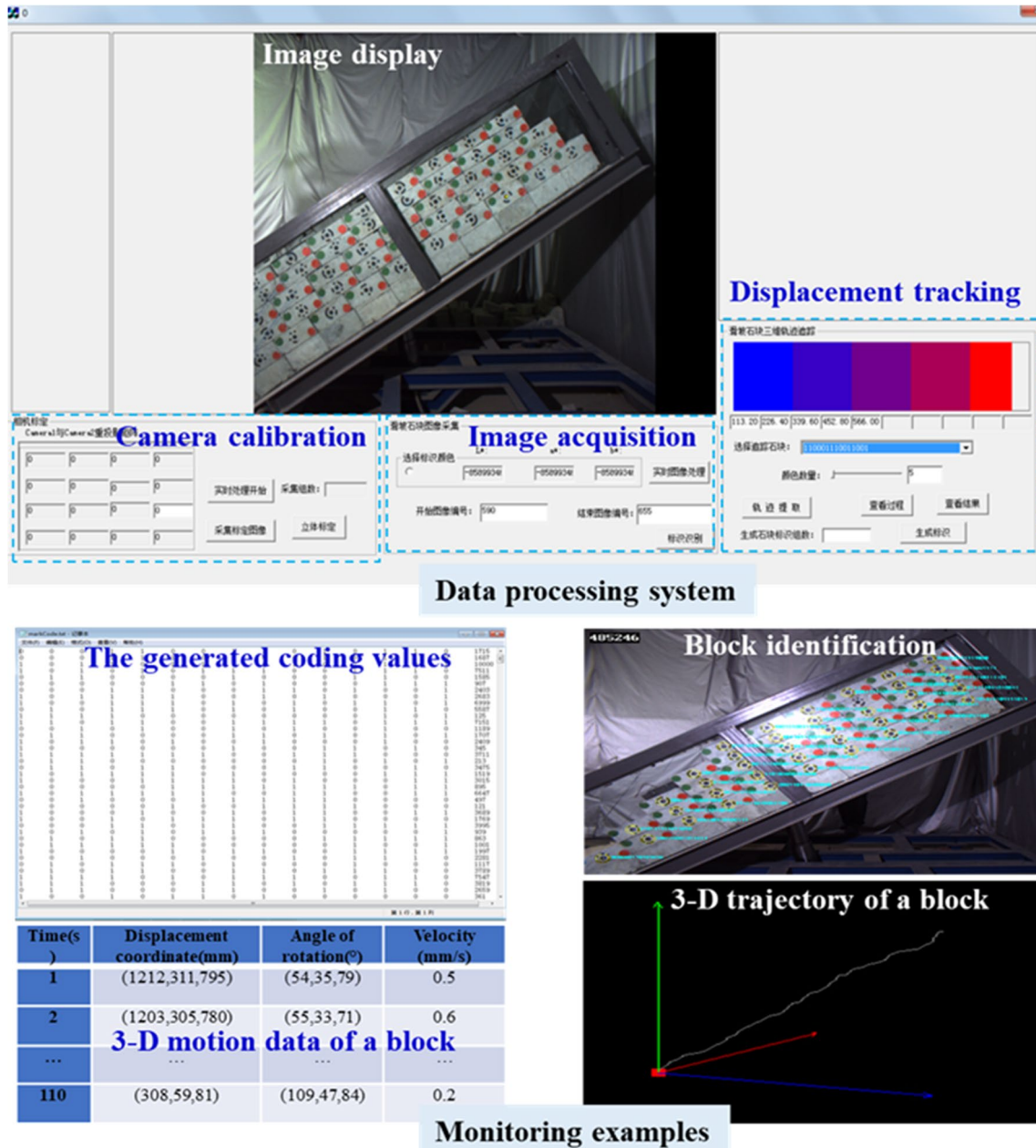


Fig. 8 Major function of the software and monitoring data of a block

Designing a physical model experiment

Model building and test scheme

The physical model experiment aimed to systematically explore the slope’s motion characteristics, deformation models, and failure mechanisms, considering the influence of structural planes’ inclination and orientation, filling conditions, slope foot excavation, etc., with a complex experiment system.

The geometry, density, and gravity similarity ratio were set to 1/50, 1, and 1, respectively. The similarity ratio of physical and mechanical parameters was calculated according to the similarity theory and presented in Table 2.

The experiment facilities comprised a model cabinet, an image acquisition system, three high-resolution video cameras, and many model blocks with significant marks. The image acquisition system has a systematic introduction in the front sections. The model cabinet dimension

was 1.2 m × 1.28 m × 2.2 m, of which three sides consisted of tempered glasses with the framework of a channel beam and one side with no constraints. The model cabinet can be rotated up and down around an axis powered by a hydraulic jack under the cabinet’s floor. The inclination angle of the base has an extensive range of variation from 0° to 60°, with an available rotation velocity of 1.0-1.5°/min.

Three groups of orthorhombic structural planes were distributed in the slope model. Planes of #3 were parallel to the floor of the model cabinet. The directions of the #2 plane varied, considering the multiple angles of $\beta=0^\circ-40^\circ$ intersecting the slope orientation. Planes of #1 were always perpendicular to #2 and #3. The dimension of the physical model experiment is presented in Fig. 9.

Test materials and rock block preparation

Many model blocks were produced, with a length and width of 20.0 cm and multiple thicknesses of 10.0 cm, 9.0 cm, 8.0 cm, and 7.0 cm, respectively. The mass ratios of water,

Table 2 Similarity relationships of the physical and mechanical parameters

Physical quantities	Similarity relationships	Similarity ratio	Physical quantities	Similarity relationships	Similarity ratio
Length	C_L	1/50	Modulus of elasticity	$C_E = C_L C_\rho C_g$	1/50
Displacement	$C_\delta = C_L C_\rho C_g$	1/50	Shear modulus	$C_G = C_L C_\rho C_g$	1/50
Unit of mass	C_ρ	1	Time	$CT = C_L^2 / C_g^2$	1/7.07
gravity	C_g	1	Stress	$C_\sigma = C_L$	1/50
Adhesion	$C_c = C_L C_\rho C_g$	1/50	Inner friction angle	C_φ	1

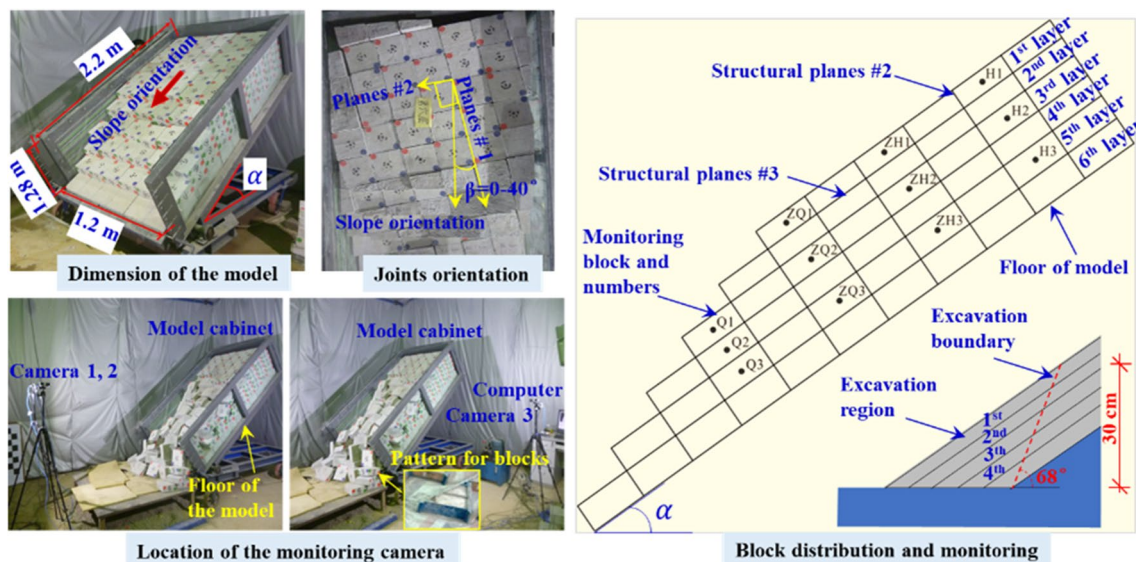


Fig. 9 Dimension and design of the physical model experiment

cement, barite powder, and gravel were designed to be 1.00:1.61:2.60:2.71, with which the unit mass of the model block was approximate to the rock block of about $\gamma = 27 \text{ kN}\cdot\text{m}^{-3}$. The cement grade was C32.5, with a gravel particle size of 0.5–1.0 cm. After the production of the block, a concrete curing period of more than 28 days was necessary. The structure plane’s inner friction angles were 24.59° without filling and 19.61° when filled with fine quartz sand, and the adhesion was tested as 4.955 kPa. The mechanical parameters approximated that of the original phyllite block.

Test scheme

A total of 10 groups of the experiment were designed. One group (No. I-1) considered the variation of dip angle, four groups (No. II-1-No. II-3) focused on the influence of filling conditions in structure planes #3, four groups (No. III-1-No. III-3) researched the effect of joint orientations, and two groups (No. IV-1-No. IV-2) studied the impact of slope foot excavation. The specific test scheme is shown in Table 3.

Motion characteristics and failure process of the slope

Disruption process and displacement characteristics

(1) Conventional condition (serial number of I-1).

Two groups of comparative tests were completed under conditions I-1, with which the dip angles of the model floor finally reached 37.8° and 36.9° , respectively.

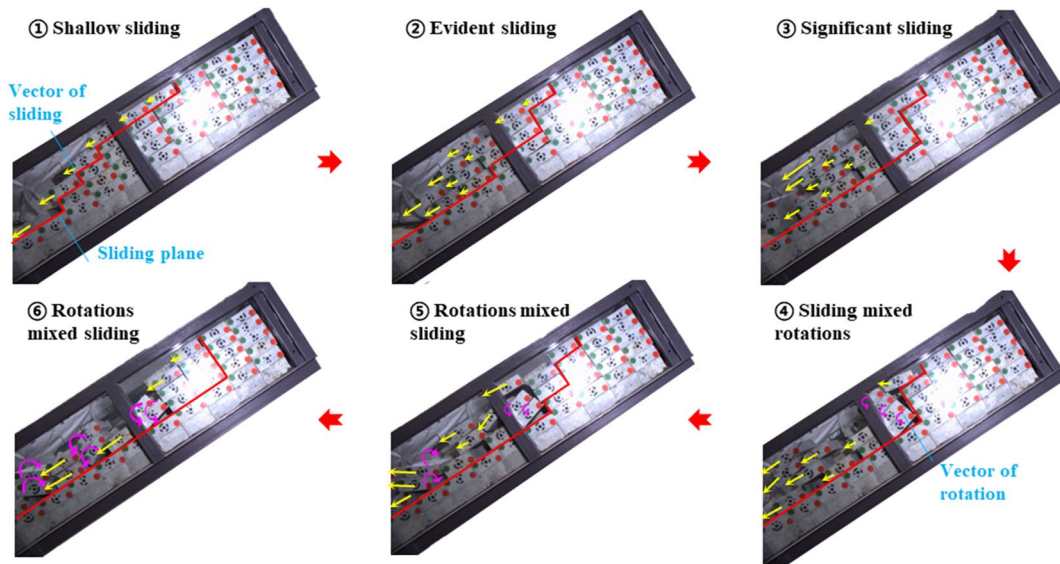
Figure 10 shows the failure process of the slope and the displacement curves. In Fig. 10 (a), we can observe that the failure process can be categorized into six stages. The first stage is shallow sliding. The sliding starts from the shallow area near the slope’s foot and shoulder. The sliding plane takes on a stepped shape. During stage 2, the sliding becomes more evident and gradually develops towards the deep and rear of the slope. Apparent displacement still concentrates in the shallow area of the slope foot, and the sliding plane gradually moves towards the deeper areas. Stage 3 is characterized by significant sliding, where the block displacements are large, and the sliding plane slowly develops towards the slope back. In Stage 4, sliding with rotation occurs. A step appears in the middle of the slope, where the blocks rotate and tilt. For Stages 5 and 6, the blocks’ movements are mainly composed of rotations and sliding along an unstable complex path, ultimately forming an L-shaped sliding plane.

Figure 10 (b) presents the blocks sliding sequence and displacement curves. Although the sliding startup time is exceptionally close, with a difference of fewer than 1.0 s, the sequence, which is the progressive destruction of the shallow, deep, and back slopes, is highly coherent. The duration of the block motion is approximately 3.0 s. The blocks in the slope’s shoulder and foot show more significant displacements. The maximum displacement is 498 mm, which is monitored from block ZQ1. The blocks near the slope back and floor, numbered Q3, ZH2, ZH3, H1, H2, and H3, show small displacements of 5.39–34.66 mm. The sliding plane gradually changes from a step shape to an L shape.

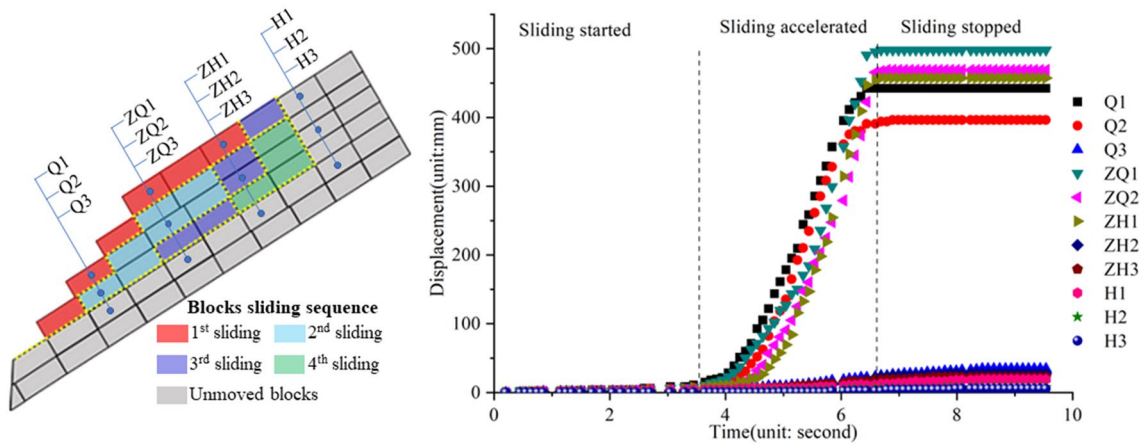
(2) Conditions of filling in structural planes #3.

Table 3 Scheme of the physical model test

Consideration	Serial number	Excavation at slope foot	Dip angle $\alpha(^{\circ})$	Joint orientation $\beta (^{\circ})$	Filling between layers	Free face at slope foot	Annotate
Conventional	I-1	No	$2^{\circ}/\text{min}$	0°	No	yes	α increased till slope destruction.
Influence of filling conditions in structure planes #3	II-1	No	$2^{\circ}/\text{min}$	0°	Filling in all planes of #3	yes	α increased till slope destruction. The filling is of fine quartz sand
	II-2	No	$2^{\circ}/\text{min}$	0°	Filling between the 2nd -3rd layers	yes	
	II-3	No	$2^{\circ}/\text{min}$	0°	Filling between the 3rd – 4th layers	yes	
Influence of Joint Orientations	III-1	No	$2^{\circ}/\text{min}$	10°	No	yes	α increased till slope destruction.
	III-2	No	$2^{\circ}/\text{min}$	20°	No	yes	Keep joints No. #1 and No. #2 orthogonal.
	III-3	No	$2^{\circ}/\text{min}$	30°	No	yes	
Influence of slope foot excavation	IV-1	Layer-by-layer excavation	35°	0°	No	No	Excavation height and dip angles were 30 cm and 68° , respectively.
	IV-2	overall foot excavation	35°	0°	No	No	



(a) The progressive process of deformation and damage (I-1)



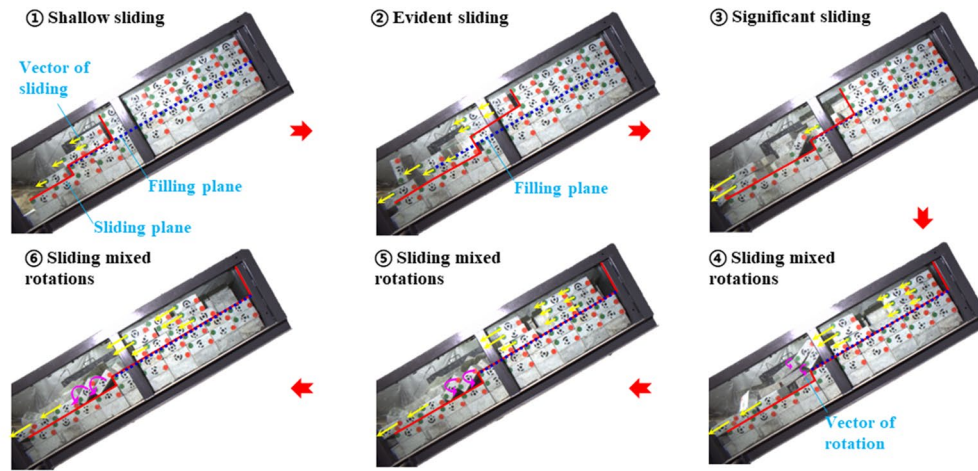
(b) The blocks sliding sequence and displacement curves (I-1)

Fig. 10 Failure process and displacement curves for condition I-1. (a) The progressive process of deformation and damage; (b) The blocks sliding sequence and displacement curves

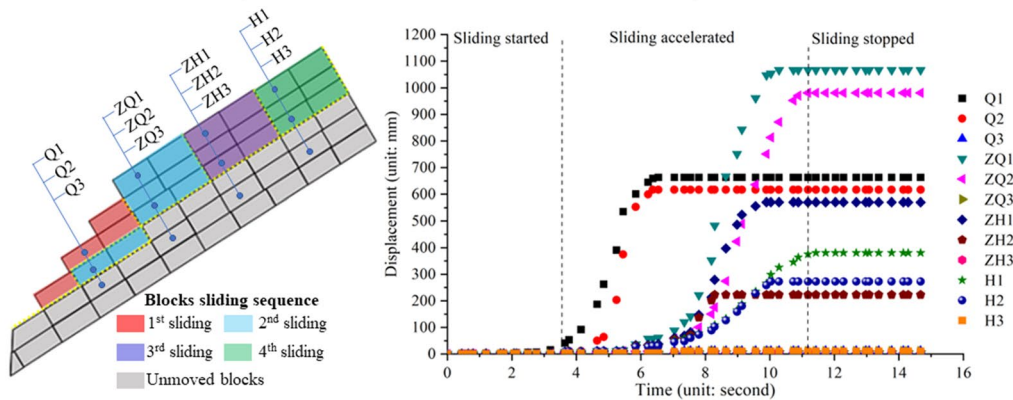
Changes in the contact planes’ strength significantly affected the blocks’ motion characteristics, including the startup time, motion duration, sliding sequences, stopping time, etc. The dip angle of the model floor finally reaches 29.0°, 31.7°, and 31.0° for tests II-1, II-2, and II-3, respectively. Compared with test I-1, the final angle significantly reduces when structural planes #3 are filled with quartz sand.

When all planes #3 are filled with quartz sand, inducing a uniform decrease in strength, the block motion features, failure progress, and deformation characteristics of test II-1 approximate the results of condition I-1. When a specific plane #3 is filled, the start/stop time and movement distance of blocks on both sides of the weakened plane are significantly different.

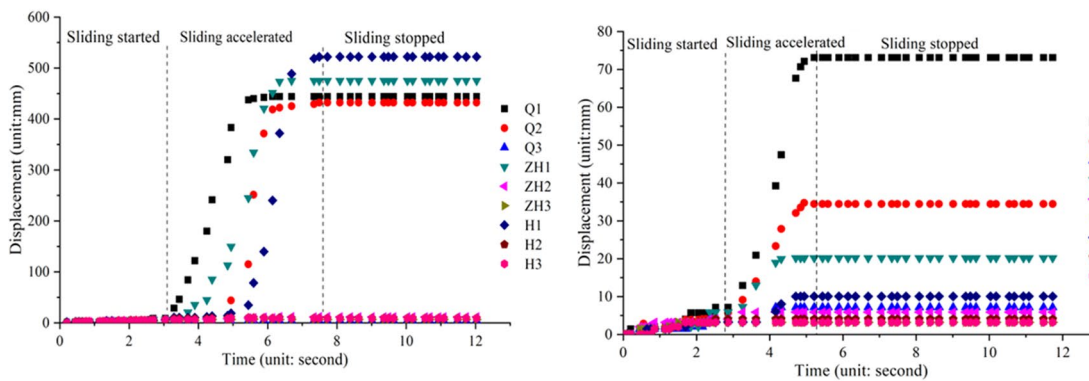
Considering the similarity of motion features and processes for tests II-1 to II-3, only group II-3 is presented in detail (Fig. 11). The results show that the sliding plane in the slope foot approximates the conventional condition (I-1). However, in the middle and rear of the slope, the sliding planes generally coincide with the preset structural plane filled with quartz sand. The sliding begins from the shallow slope foot and gradually develops deeper, and the sliding displacement decreases with the increase of burial depth. The blocks in the middle and back of the slope slide along the preset weak structural planes, with an approximate displacement for different layers of the same column. Many blocks show rotation characteristics as the sliding develops to a significant stage.



(a) The progressive process of deformation and damage (II-3)



(b) The blocks sliding sequence and displacement curves (II-3)



(c) The displacement curves for the scheme of II-1 and II-2

Fig. 11 Failure process and displacement curves for condition II. (a) The progressive process of deformation and damage (II-3); (b) The blocks' sliding sequence and displacement curves (II-3); (c) The blocks' displacement curves (II-1 and II-2)

The maximum displacement was 475 mm from block ZH1 of test II-1, 1067 mm from block ZQ1 of test II-2, and 95 mm from block Q1 of test II-3. The blocks near the shoulder are generally activated first, with larger displacements and velocities. The blocks close to the bottom and rear of the slope typically start late, with small displacements and velocities. The stopping time varies for different blocks. The

blocks above the weak plane generally slide with significant displacement.

Consequently, the reduction of structural plane strength induces the failure angle of the model floor to be more minor, the failure duration to be shorter, and the failure process to be more complicated; what's more, the slope is most likely to be unstable.

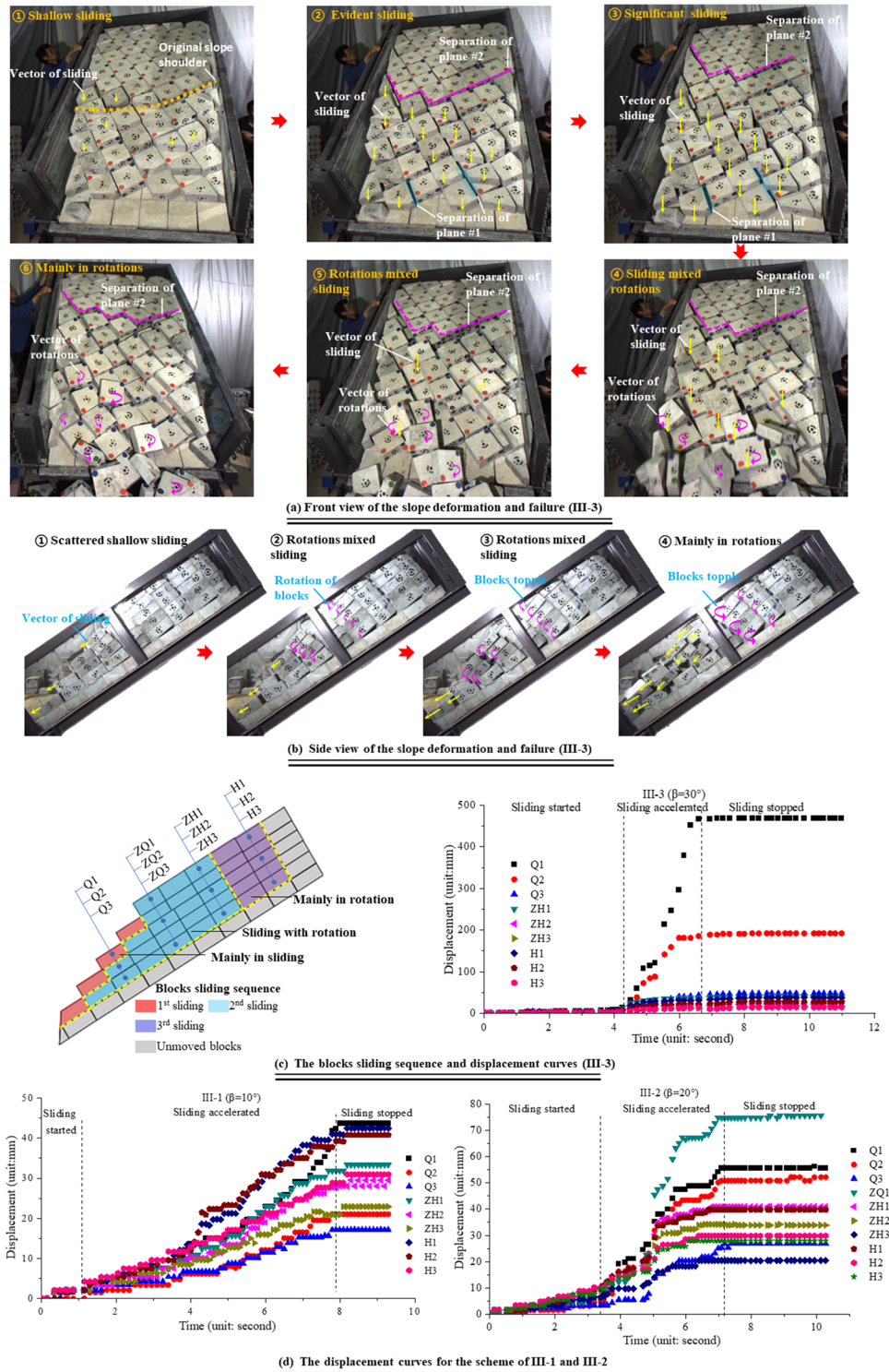
(3) Conditions of changing in orientation of planes #2.

The parameter β represents the intersection angle between slope orientation and structural plane #1. Three groups of tests were designed for comparative analysis, where the values of β are 10° , 20° , and 30° , respectively. The dip angles of the model floor finally reached 37.35° , 36.1° , and 36.05°

for the test III-1, III-2, and III-3, respectively. The influence of joint orientation on the final value of angle α was small, with a variation of less than 1.0° .

Since the tests cannot be simplified to a plane strain problem, we provide the slope's side and front damage processes. Figure 12 (a) depicts that the blocks near the

Fig. 12 Failure process and the displacement curves for condition III. (a) The progressive process of deformation and damage (III-3); (b) The blocks sliding sequence and displacement curves (III-3); (c) The block displacement curves (III-1 and III-2)



left shoulder of the slope start first, and then the middle and right blocks follow gradually; the block movement is mainly along the slope orientation in the early stage, gradually changes to rotational sliding with the increase of displacement, and is primarily in rotation in the final stage. The cross-section pictures show that the block startup order is similar to that of test I-1, but the blocks' rotations are more prominent (Fig. 12 (b)).

Figure 12 (c)-(d) compares displacement-time curves for typical blocks. The maximum displacement was 43.71 mm from block Q1 of test III-1, 75.70 mm from block ZQ1 of test III-2, and 467.92 mm from block Q1 of test III-3. The duration time of block motion was approximately 8 s, 7 s, and 2 s for tests III-1 to III-3, respectively. A relatively small block displacement and acceleration were mainly attributed to the rotation and collision of the block, which hindered the block motion.

The change in orientation of plane #1 resulted in the translation, tumbling, and rotating of blocks, which increased uncertainty and complexity in block motion.

(4) Conditions of slope foot excavation.

Foot excavation generally triggers instability and damage to the slope. The mode of soil removal, height, and dip angle of the excavation range are important factors. This study designed the excavation height and dip angle as 30 cm and 68°, respectively. The bed floor angle of the slope was a constant of 35°. Two modes of foot removal were considered: layer-by-layer excavation (test IV-1) and overall foot excavation (test IV-2).

Figure 13 presents the slope failure progress and displacement curves of typical blocks. In test IV-1, when the foot was excavated, exposing the upper two layers, the sliding was small, with a maximum displacement of 4.86 mm for the 1st layer excavation and 21.75 mm for the 2nd layer excavation. After excavating the 3rd layer, the block crept first and then accelerated sharply, and many blocks have been significantly displaced. The maximum displacement typically reached 652 mm. The excavation of the 4th layer at the slope foot stimulated the block to slide again, and the maximum displacement reached 1080 mm. The damage to the slope is progressive, progressing gradually from the front shallow to the depth and rear of the slope, with the extent of damage controlled by the excavation depth.

In test IV-2 (Fig. 14), the blocks slid slowly after the excavation, accelerated gradually to produce a large displacement up to 402.29 mm, and finally damaged the slope. In this test, the first batch of start-slip blocks were more numerous, the blocks had higher velocities and more complex kinematic characteristics, the number of rotating and tipping blocks was greater, and the time to slope failure was shorter.

Therefore, the difference in foot excavation mode affected the start sequence, acceleration process, and sliding distance of blocks.

The motion of the block was highly complex and influenced by many factors. The joint strength of structural planes affected the ultimate angle of the slope foot and the position of the sliding surface; the structural plane's orientation induced block rotations and increased the complexity; the mode of foot excavation affected the block slid sequence, locus, distance, etc.

Block acceleration and velocity characteristics

Block acceleration and velocity are critical physical quantities describing the block's motion, reflecting the conversion of potential and kinetic energy. Figure 15 presents the curves of acceleration and velocity versus motion time of typical blocks with more significant displacement.

The acceleration, velocity, and displacement recorded from the test are highly correlated. A block with more significant displacement generally shows larger velocity and acceleration. The block motion was not a linear acceleration. The waveforms were approximate to the triangular and pulse waves. The acceleration curves fluctuated significantly, with significant positive and negative amplitude. The variation in the displacement curves closely followed the acceleration. The maximum velocity of the block was recorded as 57.91, 78.70, 183.71, 19.80, 4.73, 9.96, 91.72, 49.08, 140.29, and 38.84 mm/s for tests I to IV-2, respectively. The corresponding acceleration was 33.07, 51.62, 99.28, 17.33, 4.33, 9.43, 84.55, 47.28, 78.17, and 12.54 mm/s².

Despite the significant influence of the test conditions on the acceleration and velocity, the motion of the block is a testament to the unpredictability and complexity of nature. The influence of block collision, rolling, and flipping adds to the randomness, making the waveforms extremely approximate to triangular and pulse waves.

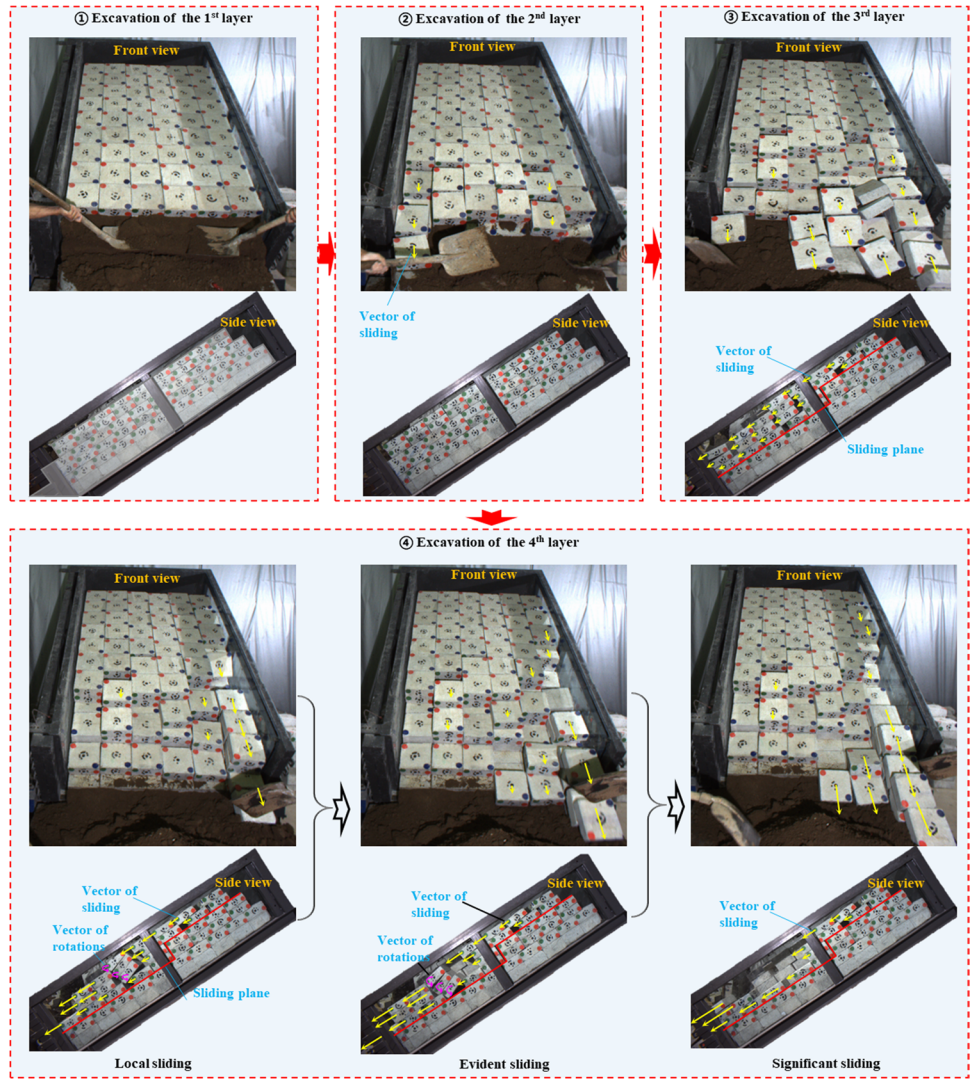
Discussion

Analysis of failure pattern and mechanism

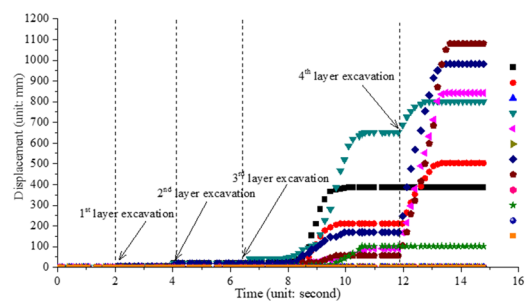
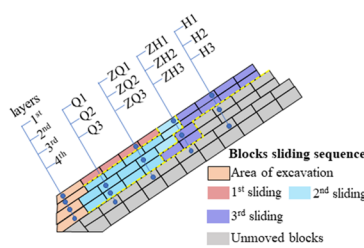
According to the starting sequences, motion loci, and accumulation characteristics of the blocks, the landslide's deformation failure model can be summarized into three types: progressive sliding failure, monolithic sliding failure, and rotary sliding failure. The schematic diagram is shown in Fig. 16.

The progressive sliding failure model mainly occurred in conventional slopes. The tensile cracks originated from the slope surface, between the blocks near the slope shoulder. The blocks detached from the rock slope, sliding or rolling along the structural plane. The sliding force was transmitted to the next layer of blocks, coupling the effects of gravity and friction driving force. The movement passed on to the

Fig. 13 Failure process and displacement curves for condition IV-1. (a) The progressive process of deformation and damage; (b) The blocks sliding sequence and displacement curves



(a) Damage characteristics of the slope



(b) Sliding sequence and displacement curves (IV-1)

deep layers gradually. The displacement, velocity, and acceleration of blocks were generally reduced from the shallow to the deep. The blocks mainly slid, accompanied by a few flipping blocks.

The monolithic sliding failure model mainly occurred in slopes with weak structural planes. The blocks near the foot of the slope first separated and slid along the soft plane. The

block movement was transmitted from the slope toe to the rear, mainly in translational motion along the soft plane with few rotations or rolling phenomena.

The rotary sliding failure model mainly occurred in slopes with complex orientations of structural planes. When the orientation of plane # 1 was not the same as the slope, the blocks in the middle part of the slope were

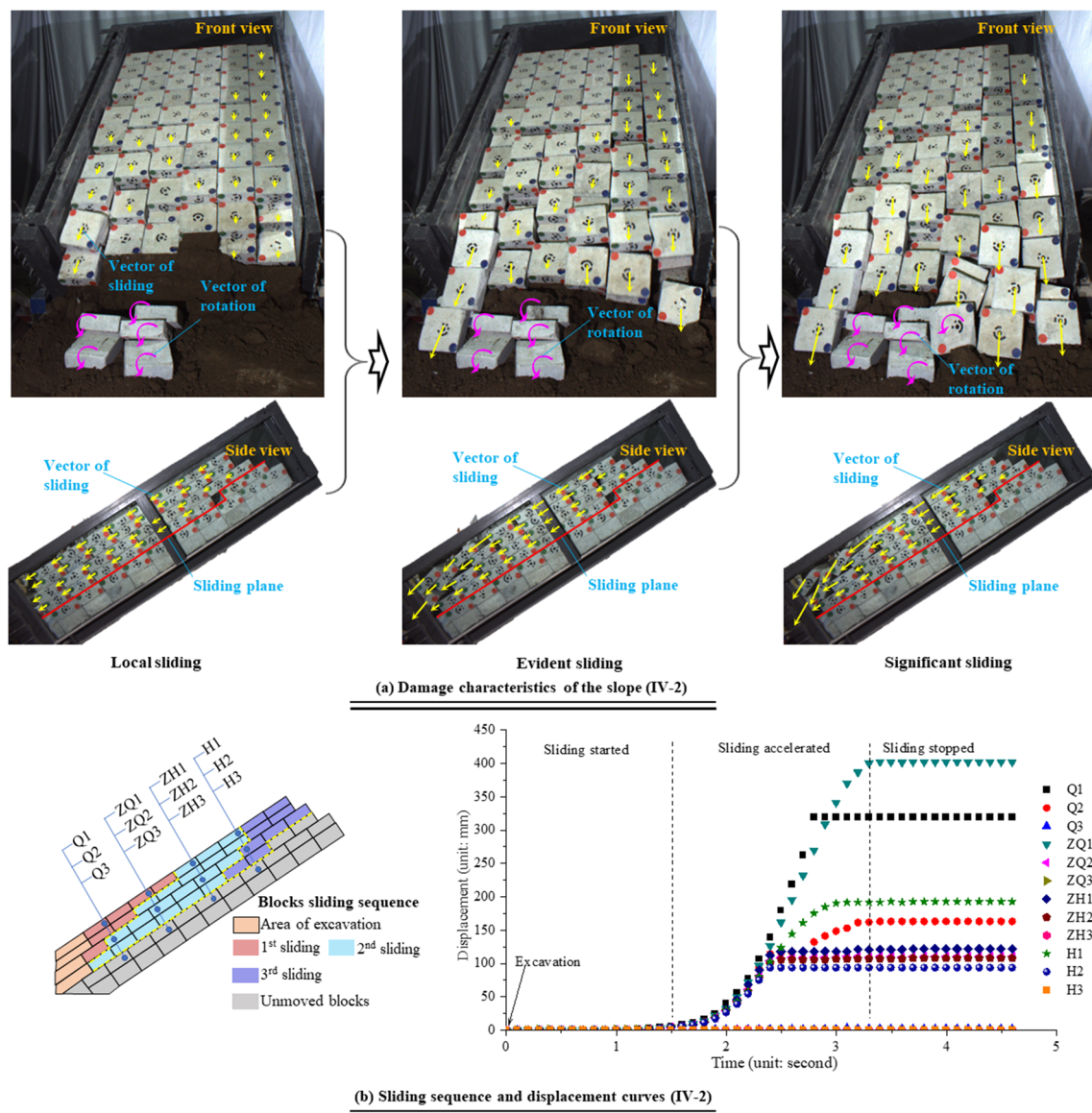


Fig. 14 Failure process and displacement curves for condition IV-2. (a) The progressive process of deformation and damage; (b) The blocks sliding sequence and displacement curves

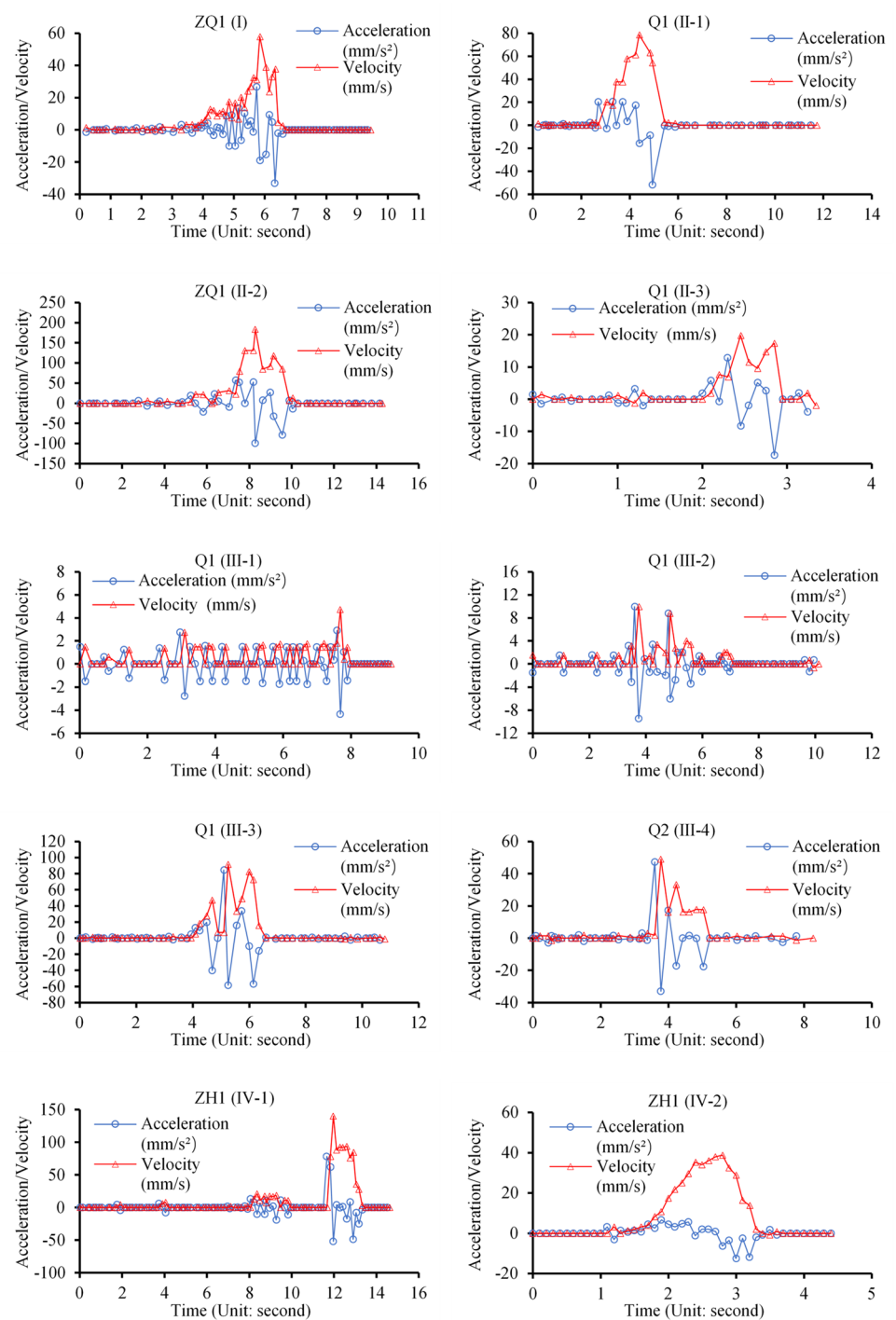
prone to slide first because only two sides were in contact with the other blocks. The blocks near both slope sides slid with rotations, accompanying a tendency to the central slope axis.

The production and monitoring of large-scale physical model experiments of rock slope failure and motion are highly complex, with many uncertainties and randomness. Although various working conditions were considered in this test, and multiple groups were repeated for each experiment, the test results remained discrete in certain. Systematic numerical simulation will be conducted for comparative analysis to explain the conclusions. However, the study could still present critical information on block motion to mitigate landslide hazards.

Significance and limitation

China’s Qinba Mountains Area presents a fragmented terrain and adverse geological structure, which is generally impacted by severe geological hazards, especially in the weak rock strata. In addition, the diversity of inducing factors and the complexity of triggering mechanisms make assessing and preventing the landslide hazards in this region very difficult. Therefore, obtaining the variation information of displacement, velocity, and acceleration during the landslide motion process is critical for the landslide hazard evaluation and risk prevention in this area. Considering the complexity of monitoring and tracking many blocks with high speed, a non-contact monitoring

Fig. 15 The curves of acceleration and velocity versus motion time of typical blocks



system was developed in this study. The Yaobai landslide was selected as the experiment prototype. A serial of large-scale model tests, considering the influence of structural planes' inclination and orientation, filling conditions, and slope foot excavation, were carried out to elucidate layered phyllite landslide's motion traits and failure mechanism. Consequently, this research's monitoring techniques and

test methods can provide scientific basis for the stability evaluation and hazard prevention of such landslides.

The production and monitoring of large-scale physical model experiments of rock slope failure and motion are highly complex, with many uncertainties and randomness. Although various working conditions were considered in this test, and multiple groups were repeated for each experiment,

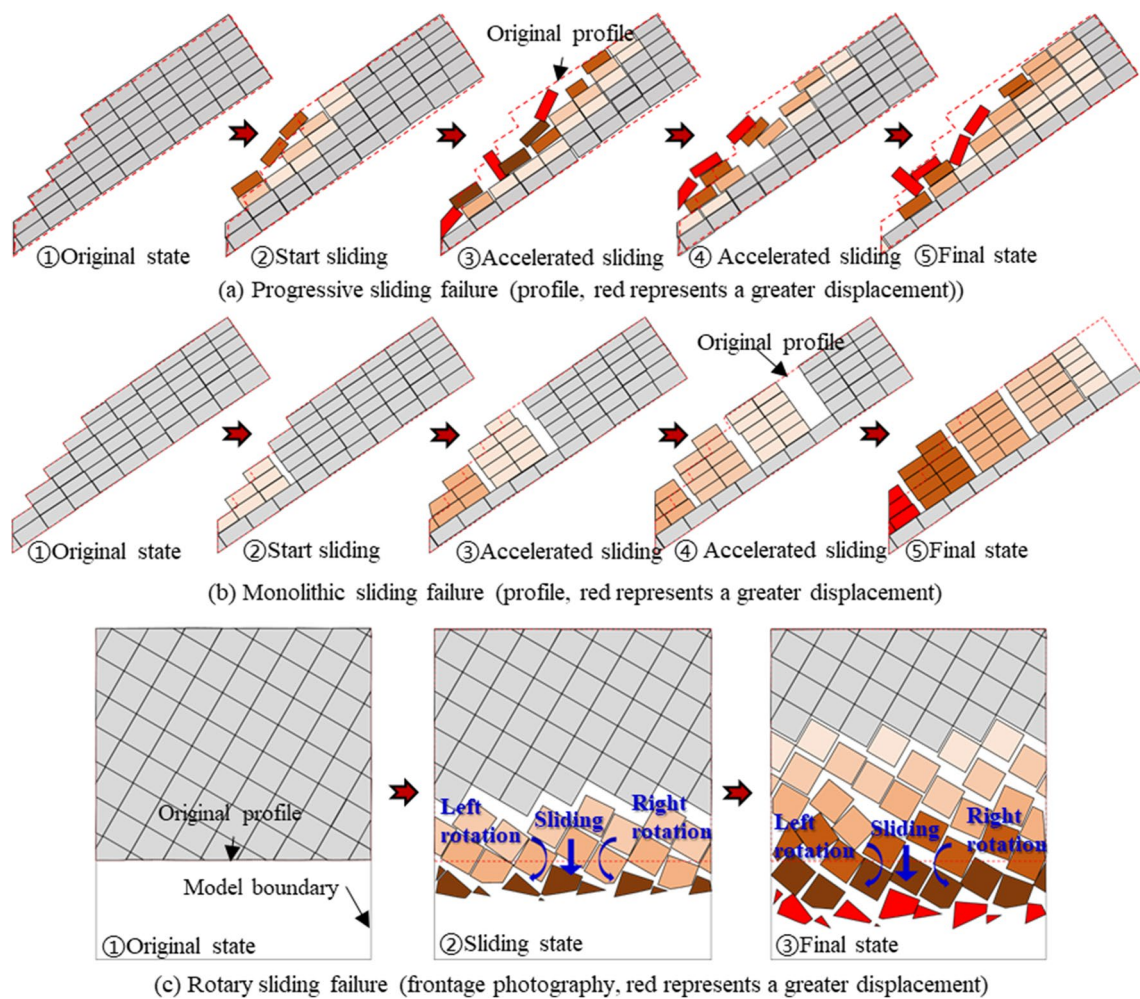


Fig. 16 Types of landslide failure and motion

the test results remained discrete in certain. As the fracture zone and weak interface within the slope, the structural planes control the formation of the potential sliding surface and the ultimate angle of the slope foot. This study’s design of structural planes and rock blocks is mainly regular and uniform, which are different from the complex structural planes and irregular phyllite rocks in actual slopes. Additionally, the variation of stress within the slope was not monitored during the test, which was not comprehensive enough. Therefore, to understand the motion characteristics and damage mechanisms of layered phyllite landslide in the Qinba Mountains Area more comprehensively, we put forward the following ideas for future research: (1) Systematic numerical simulation will be conducted for comparative analysis to explain the conclusions. Through numerical simulation, the characteristics and variation rules of more parameters during slope movement can be obtained. (2) Improve the accuracy of the monitoring system and introduce the detection means with high precision.

Conclusion

Taking the Yaobai landslide in Bailiu Town of Shaanxi Xunyang County, as an example, the landslide’s block motion and damage mechanism were elucidated. The research results are as follows:

- (1) A non-contact monitoring system was developed, with which the large-scale physical model tests were carried out to monitor the transient block motion and elucidate the slope’s failure mechanism. The influence of structural planes’ inclination and orientation, filling conditions, slope foot excavation, etc., was considered.
- (2) The block’s motion was extremely complex and influenced by many factors. The structural planes’ strength affected the ultimate angle of the slope foot and the position of the sliding plane; the structural planes’ orientation induced block rotations and increased the

complexity; the mode of foot excavation affected the block slid sequence, locus, distance, etc.

- (3) Although the test conditions significantly affected the acceleration and velocity, the motion was full of randomness and complexity due to the influence of the block collision, rolling, and flipping. The waveforms were extremely approximate to triangular and pulse waves.
- (4) According to the starting sequences, motion loci, and accumulation characteristics of the block, the landslide's deformation failure model can be summarized into three types: progressive sliding failure, monolithic sliding failure, and rotary sliding failure.

The block velocity, acceleration, displacement, and damage characteristics monitored by the model test can provide a basis for evaluating the Yaobai landslide. The research results can provide a basis for preventing and controlling such landslides.

Funding This study was sponsored by the National Key & Program of China (Grant numbers 2022YFC3003403) and the National Natural Science Foundation of China (grant numbers 42220104005 and 41877245). The Department of Science and Technology of Shaanxi Province (grant numbers 2019ZDLSF07-0701).

Data availability The original contributions presented in this study are included in the article, and further inquiries can be directed to the corresponding author.

Declarations

Conflict of interest The authors declare that they have no conflicts of interest.

CRedit authorship contribution statement Yanbo Cao: investigation, writing-original draft, writing- review & editing, data curation. Longsheng Deng: conceptualization, methodology, investigation, writing-original draft, writing- review & editing, data curation, format analysis. Wen Fan: conceptualization, methodology, supervision. Dong Tang: writing-original draft. Jiale Chen: writing-original draft. Bin Zheng: investigation.

References

- Alvarado M, Pinyol NM, Alonso EE (2019) Landslide motion assessment including rate effects and thermal interactions: revisiting the Canelles landslide. *Can Geotech J* 56(9):1338–1350. <https://doi.org/10.1139/cgj-2018-0779>
- Corominas J (1996) The angle of reach as a mobility index for small and large landslides. *Can Geotech J* 33(2):260–271. <https://doi.org/10.1139/t96-005>
- Cruden DM (1991) A simple definition of a landslide. *Bulletin of the International Association of Engineering Geology-Bulletin de l'Association Internationale de Géologie de l'Ingénieur* 43(1):27–29. <https://doi.org/10.1007/BF02590167>
- Cui P, Zhu YY, Han YS, Chen XQ, Zhuang JQ (2009) The 12 May Wenchuan earthquake-induced landslide lakes: distribution and preliminary risk evaluation. *Landslides* 6(3):209–223. <https://doi.org/10.1007/s10346-009-0160-9>
- Dai FC, Lee CF, Ngai YY (2002) Landslide risk assessment and management: an overview. *Eng Geol* 64(1):65–87. [https://doi.org/10.1016/S0013-7952\(01\)00093-X](https://doi.org/10.1016/S0013-7952(01)00093-X)
- Deng L, Fan W, Yu M (2018) Parametric study of a loess slope based on unified strength theory. *Eng Geol* 2018:233. <https://doi.org/10.1016/j.enggeo.2017.11.009>
- Deng Y, He S, Scaringi G, Lei X (2020) Mineralogical analysis of selective melting in partially coherent rockslides: bridging solid and molten friction. *J Geophys Research: Solid Earth* 125(8):e2020JB019453. <https://doi.org/10.1029/2020JB019453>
- Fan W, Wei Y, Deng L (2018) Failure modes and mechanisms of shallow debris landslides using an artificial rainfall model experiment on Qin-Ba Mountain. *Int J Geomech* 18(3):04017157. [https://doi.org/10.1061/\(ASCE\)GM.1943-5622.0001068](https://doi.org/10.1061/(ASCE)GM.1943-5622.0001068). -1-13
- Fan W, Lv J, Cao Y, Shen M, Deng L, Wei Y (2019) Characteristics and Block Kinematics of a Fault-Related Landslide in Qinba Mountains Western China. *Eng Geol* 249:162–171. <https://doi.org/10.1016/j.enggeo.2018.12.019>
- Fan X, Tang J, Tian S, Jiang Y (2020) Rainfall-induced rapid and long-runout catastrophic landslide on July 23, 2019 in Shuicheng, Guizhou, China. *Landslides* 17(9):2161–2171. <https://doi.org/10.1007/s10346-020-01454-y>
- Gao Y, Li B, Gao H, Chen L, Wang Y (2020) Dynamic characteristics of high-elevation and long-runout landslides in the Emeishan basalt area: a case study of the Shuicheng 7.23 landslide in Guizhou. *China Landslides* 17(7):1663–1677. <https://doi.org/10.1007/s10346-020-01377-8>
- Iverson RM (2005) Regulation of landslide motion by dilatancy and pore pressure feedback. *J Geophys Research: Earth Surf* 110. <https://doi.org/10.1029/2004JF000268>
- Keefer DK (1984) Rock avalanches caused by earthquakes: source characteristics. *Science* 223(4642):1288–1290. <https://doi.org/10.1126/science.223.4642.1288>
- Lan H, Tian N, Li L, Wu Y, Macciotta R, Clague J (2022a) Kinematic-based landslide risk management for the Sichuan-Tibet Grid Interconnection Project (STGIP) in China. *Eng Geol* 308:106823. <https://doi.org/10.1016/j.enggeo.2022.106823>
- Lan H, Zhang Y, Macciotta R, Li L, Wu Y, Bao H, Peng J (2022b) The role of discontinuities in the susceptibility, development, and runout of rock avalanches: a review. *Landslides* 19:1391–1404. <https://doi.org/10.1007/s10346-022-01868-w>
- Li Y, Wang X, Mao H (2020) Influence of human activity on landslide susceptibility development in the three gorges area. *Nat Hazards* 104(3):2115–2151. <https://doi.org/10.1007/s11069-020-04264-6>
- McDougall S, Hungr O (2004) A model for the analysis of rapid landslide motion across three-dimensional terrain. *Can Geotech J* 41(6):1084–1097. <https://doi.org/10.1139/t04-052>
- Persichillo MG, Bordoni M, Cavalli M, Crema S, Meisina C (2018) The role of human activities on sediment connectivity of shallow landslides. *CATENA* 160:261–274. <https://doi.org/10.1016/j.catena.2017.09.025>
- Qi S, Xu Q, Zhang B, Zhou Y, Lan H, Li L (2011) Source characteristics of long runout rock avalanches triggered by the 2008 Wenchuan earthquake, China. *J Asian Earth Sci* 40(4):896–906. <https://doi.org/10.1016/j.jseaeas.2010.05.010>
- Qiu H, Cui Y, Hu S, Yang D, Pei Y, Yang W (2019) Temporal and spatial distributions of landslides in the Qinba Mountains, Shaanxi Province, China. *Geomatics. Nat Hazards Risk* 10(1):599–621. <https://doi.org/10.1080/19475705.2018.1536080>
- Scaioni M, Longoni L, Melillo V, Papini M (2014) Remote sensing for landslide investigations: an overview of recent achievements

- and perspectives. *Remote Sens* 6(10):9600–9652. <https://doi.org/10.3390/rs6109600>
- Soldato MD, Solari L, Poggi F, Raspini F, Tomás R, Fanti R, Casagli N (2019) Landslide-induced damage probability estimation coupling InSAR and field survey data by fragility curves. *Remote Sens* 11(12):1486. <https://doi.org/10.3390/rs11121486>
- Tang C, Zhu J, Qi X, Ding J (2011) Landslides induced by the Wenchuan earthquake and the subsequent strong rainfall event: a case study in the Beichuan area of China. *Eng Geol* 122(1–2):22–33. <https://doi.org/10.1016/j.enggeo.2011.03.013>
- Tsangaratos P, Ilia I, Hong H, Chen W, Xu C (2017) Applying information theory and GIS-based quantitative methods to produce landslide susceptibility maps in Nancheng County, China. *Landslides* 14(3):1091–1111. <https://doi.org/10.1007/s10346-016-0769-4>
- Wang F, Sassa K (2010) Landslide simulation by a geotechnical model combined with a model for apparent friction change. *Physics and Chemistry of the Earth. Parts A/B/C* 35(3–5):149–161. <https://doi.org/10.1016/j.pce.2009.07.006>
- Wang Y, Qi W, Zhou Y, Jin J, Liu Y, Zhao F (2015) Qiao Ergou landslide formation mechanism and characteristics. *Engineering Geology for Society and Territory*-volume 2. Springer, Cham, pp 1383–1387. https://doi.org/10.1007/978-3-319-09057-3_244
- Wang YF, Cheng QG, Lin QW, Li K, Yang HF (2018) Insights into the kinematics and dynamics of the Luanshibao rock avalanche (Tibetan Plateau, China) based on its complex surface landforms. *Geomorphology* 317:170–183. <https://doi.org/10.1016/j.geomorph.2018.05.025>
- Wei X, Fan W, Cao Y, Chai X, Bordoni M, Meisina C, Li J (2019a) Integrated experiments on field monitoring and hydro-mechanical modeling for determination of a triggering threshold of rainfall-induced shallow landslides. A case study in Ren River catchment, China. *Bull Eng Geol Environ* 79(1):513–532. <https://doi.org/10.1007/s10064-019-01570-7>
- Wei J, Zhao Z, Xu C, Wen Q (2019b) Numerical investigation of landslide kinetics for the recent mabian landslide (Sichuan, China). *Landslides* 16(11):2287–2298. <https://doi.org/10.1007/s10346-019-01237-0>
- Wei X, Fan W, Chai X, Cao Y (2020) Field and numerical investigations of triggering mechanism in typical rainfall-induced shallow landslides: a case study in the Ren River catchment, China. *Nat Hazards* 103(2):2145–2170. <https://doi.org/10.1007/s11069-020-01570-2>
- Xing AG, Wang G, Yin YP, Jiang Y, Wang GZ, Yang SY, Dai DR, Zhu YO, Dai JA (2014) Dynamic analysis and field investigation of a fluidized landslide in Guanling. *Guizhou China Eng Geol* 181:1–14. <https://doi.org/10.1016/j.enggeo.2014.07.022>
- Xu Q, Zhang S, Li W (2011) Spatial distribution of large-scale landslides induced by the 5.12 Wenchuan earthquake. *J Mt Sci* 8(2):246–260. <https://doi.org/10.1007/s11629-011-2105-8>
- Xu C, Dai F, Xu X, Lee YH (2012) GIS-based support vector machine modeling of earthquake-triggered landslide susceptibility in the Jianjiang River watershed, China. *Geomorphology* 145:70–80. <https://doi.org/10.1016/j.geomorph.2011.12.040>
- Yin Y, Wang F, Sun P (2009) Landslide hazards triggered by the 2008 Wenchuan earthquake. *Sichuan China Landslides* 6(2):139–152. <https://doi.org/10.1007/s10346-009-0148-5>
- Yin Y, Xing A, Wang G, Feng Z, Li B, Jiang Y (2017) Experimental and numerical investigations of a catastrophic long-runout landslide in Zhenxiong, Yunnan, southwestern China. *Landslides* 14(2):649–659. <https://doi.org/10.1007/s10346-016-0729-z>
- Zhang H, Deng Y, Zhang Z, He S (2022) Power density-dependent friction weakening for long-runout landslides and its revelation of volume and topographical effects. *Acta Geotech* 1–11. <https://doi.org/10.1007/s11440-022-01644-z>
- Zhou J, Zhao F, Zhu Y, Dong W, He Z (2021) Dynamic behavior and constitutive relationship of Mudstone Slip Zone of landslide with weak interlayer. *Shock Vib* 2021. <https://doi.org/10.1155/2021/3330127>

Publisher's note Springer Nature remains neutral with regard to jurisdictional claims in published maps and institutional affiliations.